In situ small-angle X-ray scattering reveals solution phase discharge of Li–O_2 batteries with weakly solvating electrolytes

Christian Prehal[a,b,1], Aleksej Samojlov[a], Manfred Nachtnebel[c], Ludek Lovicar[d], Manfred Kriechbaum[e], Heinz Amenitsch[e], and Stefan A. Freunberger[a,d,1]

[a]Institute for Chemistry and Technology of Materials, Graz University of Technology, 8010 Graz, Austria; [b]Department of Information Technology and Electrical Engineering, ETH Zürich, 8092 Zürich, Switzerland; [c]Institute of Electron Microscopy and Nanoanalysis and Graz Centre for Electron Microscopy (FELMI-ZFE), Graz University of Technology, 8010 Graz, Austria; [d]Institute of Science and Technology Austria, 3400 Klosterneuburg, Austria; and [e]Institute of Inorganic Chemistry, Graz University of Technology, 8010 Graz, Austria

Edited by Alexis T. Bell, University of California, Berkeley, CA, and approved March 3, 2021 (received for review October 20, 2020)

Electrodepositing insulating lithium peroxide (Li_2O_2) is the key process during discharge of aprotic Li–O_2 batteries and determines rate, capacity, and reversibility. Current understanding states that the partition between surface adsorbed and dissolved lithium superoxide governs whether Li_2O_2 grows as a conformal surface film or larger particles, leading to low or high capacities, respectively. However, better understanding governing factors for Li_2O_2 packing density and capacity requires structural sensitive in situ metrologies. Here, we establish in situ small- and wide-angle X-ray scattering (SAXS/WAXS) as a suitable method to record the Li_2O_2 phase evolution with atomic to submicrometer resolution during cycling a custom-built in situ Li–O_2 cell. Combined with sophisticated data analysis, SAXS allows retrieving rich quantitative structural information from complex multiphase systems. Surprisingly, we find that features are absent that would point at a Li_2O_2 surface film formed via two consecutive electron transfers, even in poorly solvating electrolytes thought to be prototypical for surface growth. All scattering data can be modeled by stacks of thin Li_2O_2 platelets potentially forming large toroidal particles. Li_2O_2 solution growth is further justified by rotating ring-disk electrode measurements and electron microscopy. Higher discharge overpotentials lead to smaller Li_2O_2 particles, but there is no transition to an electronically passivating, conformal Li_2O_2 coating. Hence, mass transport of reactive species rather than electronic transport through a Li_2O_2 film limits the discharge capacity. Provided that species mobilities and carbon surface areas are high, this allows for high discharge capacities even in weakly solvating electrolytes. The currently accepted Li–O_2 reaction mechanism ought to be reconsidered.

small-angle X-ray scattering | oxygen reduction | disproportionation | Li-air battery

Understanding formation, properties, and function of energy materials requires not only information about chemistry but even more so about structure from atomic to μm scales (1), which puts high demands on (in situ) analytical techniques (2). This is the more important as complex composites and transformations are concerned (3). Electrodeposition of insulators is an intriguing example, where anything between monolayers and micrometric layers may form, even though the process is, in principle, self-limited to the electron tunneling distance of the deposit (4, 5). Topical examples are Li–S batteries, where Li_2S/S_8 are electrodeposited on discharge/charge (6) and Li–O_2 batteries, where insoluble and insulating lithium peroxide (Li_2O_2) is electrodeposited on discharge and the process being reversed on charge (5). Li–O_2 batteries could surpass current Li-ion batteries in energy, sustainability, and cost (4). However, practically realizing high reversible capacities faces the challenges of forming/decomposing large amounts of Li_2O_2 while suppressing parasitic reactions (5, 7–11). These challenges are interrelated and require understanding the interplay between physical chemistry and structural evolution at the nanoscale (2, 12–16).

Currently, the discharge process of Li–O_2 batteries is understood to proceed in between two limiting cases, governed by the electrolyte solubility of the lithium superoxide (LiO_2) intermediate (5, 17–22). If LiO_2 is soluble, it is mobile and disproportionates remote from the pore surface to form typically some 100 nm large particles, allowing for high capacities (17, 18, 22, 23). In electrolytes where LiO_2 is thought insoluble, Li_2O_2 would grow as thin passivating surface film (24–28), leading to poor rates and low capacity (*SI Appendix*, Fig. S1). The prevailing mechanism not only determines rate and capacity (5, 7, 17–19, 28–30) but also impacts parasitic chemistry (7, 17, 31–33). However, the extent to which these mechanisms prevail is still not clear, and so is the true capacity-limiting factor, which could be either e^- transport through a thin Li_2O_2 coating or mass transport (O_2, LiO_2, and Li^+) through a porous particulate Li_2O_2 deposit (25, 28, 30, 34–36). Measures and governing factors for Li_2O_2 packing density and capacity still need refinement. Conclusively identifying capacity limitations requires real-time in situ metrologies with structural sensitivity from the atomic to submicron scale. Current techniques are strong in aspects but fail to

Significance

Lithium–air batteries are promising next-generation energy storage devices and operate by electrodepositing insulating lithium peroxide (Li_2O_2). Understanding how large amounts of Li_2O_2 form, corresponding to large capacities, and what limits the amount is therefore paramount and requires following its structural evolution from atomic to micron scales. We demonstrate that in situ small- and wide-angle X-ray scattering together with sophisticated data evaluation provides access to these scales. This allows distinguishing the two reported competing reaction mechanisms, which are thought to be responsible for large and small capacities, respectively. We find that, surprisingly, only one pathway predominates at all conditions. On a wider perspective, we introduce a powerful tool to characterize transformations in complex multiphase materials.

Author contributions: C.P. and S.A.F. designed research; C.P., A.S., M.N., L.L., M.K., and S.A.F. performed research; C.P., H.A., and S.A.F. contributed new reagents/analytic tools; C.P. and S.A.F. analyzed data; and C.P. and S.A.F. wrote the paper.

The authors declare no competing interest.

This article is a PNAS Direct Submission.

[1]To whom correspondence may be addressed. Email: cprehal@ethz.ch or stefan.freunberger@ist.ac.at.

This article contains supporting information online at https://www.pnas.org/lookup/suppl/doi:10.1073/pnas.2021893118/-/DCSupplemental.

Published March 30, 2021.

seamlessly cover the required length scales in the crucial in situ fashion (2, 37). Small- and wide-angle X-ray scattering (SAXS/WAXS) could in principle afford this because of its sensitivity toward any means that generate electron density contrast on length scales from 0.1 to 100 nm. However, SAXS data analysis from complex systems is highly challenging.

Here, we expand the possibilities of in situ SAXS by developing a data analysis strategy that makes accessible the rich quantitative information contained in the scattering data of the electrochemical multiphase systems. The strategy includes 1) generating a statistically representative three-dimensional (3D) model of the electrode and 2) growth of Li_2O_2 structures by a suitable growth model, which we validate against measured scattering curves. We start with showing that in a high surface area carbon, a heuristic nucleation and growth model of thin Li_2O_2 platelets fits the in situ SAXS data over a range of electrolytes, voltages, and currents including such thought to be prototypical for surface or solution growth. Crucially, this method allows widely excluding a conformal Li_2O_2 coating to grow even in poorly solvating electrolytes and at high overpotentials; conditions previously considered prototypical for surface growth. This implies the capacity to be conclusively limited by species (O_2, LiO_2, and Li^+) transport through the porous particulate Li_2O_2 deposit rather than electronic transport limitation through a conformal Li_2O_2 coating. Rotating ring-disk electrode (RRDE) measurements and electron microscopy independently justify solution-mediated discharge in weakly solvating electrolytes. The study provides 1) unexpected insights linking the nanoscale structure with Li–O_2 mechanisms and performance and 2) the in situ metrology tool to quantitatively characterize morphologies and growth mechanisms in complex multiphase systems in general, not limited to batteries or electrochemistry.

Results and Discussion

In Situ SAXS/WAXS. Given the known prominent role of LiO_2 solvation on product growth, we chose electrolytes that span the whole range from mostly associated to dissociated LiO_2. These are 1) acetonitrile (MeCN) as prototype electrolyte believed to form Li_2O_2 as a conformal coating via surface growth (18, 20), 2) dimethylacetamide (DMAc) with intermediate solvation (18, 20), and 3) tetraethyleneglycol dimethylether (TEGDME) containing 4,000 ppm H_2O as a prototype electrolyte to form large toroidal Li_2O_2 particles via solution growth. In accord with the majority of works in literature (5, 7, 38), we refer to surface growth as the process that produces a (conformal) Li_2O_2 film on the substrate via two consecutive electron transfers limited to the electron tunneling/conduction thickness, often considered around 7 nm (5, 25, 26, 39, 40). The exact number depends on the applied current (41), the potential (42), the concentration of defects or Li_2O_2 crystallinity (40, 43), the homogeneity of the film (44), and the presence of catalysts (45). Yet, the morphology is expected to be film like, as the particle thickness growth is self-limited by the drastic increase in resistivity with increasing thickness (46). The salient feature of Li_2O_2 solution growth is that the second electron transfer passes via LiO_2 disproportionation $2\,LiO_2 \rightarrow Li_2O_2 + O_2$ (5). Note that we do not imply whether the LiO_2 diffused through the solution or at the surface of existing Li_2O_2 crystallites. Since even small amounts of water in low-DN electrolytes could strongly alter product growth (17), we meticulously excluded any unintended water contamination as detailed in *SI Appendix*, Supplementary Note 1. As cathode material, we used the nanoporous KetjenBlack (KB) carbon black with a high Brunauer-Emmett-Teller (BET) area of 1,398 $m^2 \cdot g^{-1}$.

Understanding the contribution of Li_2O_2 surface growth to capacity limitation requires in situ metrologies sensitive to Li_2O_2 phase evolution with feature sizes from the atomic to the submicron scale. To meet all these requirements, we employed in situ SAXS/WAXS. A custom-built in situ Li–O_2 battery (as detailed in *Materials and Methods* and shown in Fig. 1*A*, sketch of the cell assembly in *SI Appendix*, Fig. S2) assures unperturbed cathode performance as confirmed by capacities equivalent to laboratory cells (compare Fig. 1 and *SI Appendix*, Figs. S3*A* and S4). A small, 2 mm hole in anode and separator guaranteed that the cathode was the only active cell component hit by the X-ray beam. SAXS and WAXS intensities were recorded simultaneously on a two-dimensional (2D) areal detector in an in-house SAXS machine.

Contrary to what current understanding would suggest, achieved discharge capacities (at 0.007 $\mu A \cdot cm_{real}^{-2}$ and ~2.7 V versus Li/Li^+) with the three electrolytes during the in situ experiments do not follow the order of highest capacity with the highest degree of LiO_2 dissociation (Fig. 1*B*); the poorly dissociating MeCN electrolyte gives the highest capacity, highly dissociating TEGDME/H_2O the lowest capacities. Quantifying the structural evolution of active material may help to understand these unexpected performance relations.

Considering first the WAXS data, (100), (101), and (102) diffraction peaks emerge in all electrolytes, confirming crystalline Li_2O_2 to form in all experiments (Fig. 1 *C*–*E*). Differences in the integral peak intensities of the three electrolytes indicate different amounts of deposited Li_2O_2. This can be explained by the significantly different discharge capacities (Fig. 1*B*) and different Li_2O_2 yields (17). The large difference between (100) and (101) peak widths could be either caused by eminently anisotropic crystallite shapes or anisotropic nonuniform strain. However, recent in situ X-ray diffraction (XRD) (47, 48) (combined with Rietveld analysis) and electron microscopy studies (49–51) reveal thin disk-like Li_2O_2 crystallites (Fig. 1*F*) induced by anisotropic surface energies of the Li_2O_2 crystal facets (52). Lorentzian peak fit parameters are given in *SI Appendix*, Fig. S5. For TEGDME/H_2O, the peak widths differ less, indicating slightly thicker Li_2O_2 platelets. Beyond this information, WAXS cannot make a statement about the ordering in between the crystallites, the position toward the carbon surface, and to what extent Li_2O_2 grows in the form of a thin conformal coating.

SAXS, in contrast, contains this missing information because of its sensitivity toward any means that generate electron density contrast between <1 to ~100 nm (depending on the accessible angle range). The data contains hence rich structural and kinetic information, but inferring back to the complex multiphase system (carbon + Li_2O_2 + electrolyte) is highly challenging. Analytical SAXS models could in principle describe the ordering and arrangement of infinitely extended platelets (53), spheres, or the like. However, these models do not account for the scattering contribution of carbon and the limited expansion of Li_2O_2 particles. To exploit the data, we present a data analysis strategy (Fig. 2) that is generally applicable to complex multiphase systems and based on previous work developed for supercapacitors (54, 55). It allows for following the Li_2O_2 phase evolution in situ and extracting nucleation/growth parameters using a suitable Li_2O_2 growth model.

First, we generate a statistically representative stochastic model of the carbon on a 3D lattice. Using an intersected Boolean model (56), we generate a scattering curve, which is fitted to the ex situ SAXS curve of the dry electrode (Fig. 2 *A* and *B* and *SI Appendix*, Fig. S6). Then, the 3D carbon structure (400^3 voxels with 0.75 nm^3) is reproduced with these fit parameters. Its Fast Fourier Transformation (FFT) yields the scattering curve, which verifies the derived structure with respect to the modeled SAXS intensity. Details are given in *Materials and Methods*. Second, the carbon structure is filled with Li_2O_2 using any appropriate algorithm to model possible morphologies arising from surface growth (a conformal Li_2O_2 coating) or solution growth (Li_2O_2 platelets) (Fig. 2*C*). Whether the grown morphology is representative of the one experimentally obtained is checked by generating the corresponding scattering curve using FFT (Fig. 2*D*) and comparing it with the measured curve (Fig. 2*E*). This way, model parameters such as nucleation and growth rates can be fitted to best match

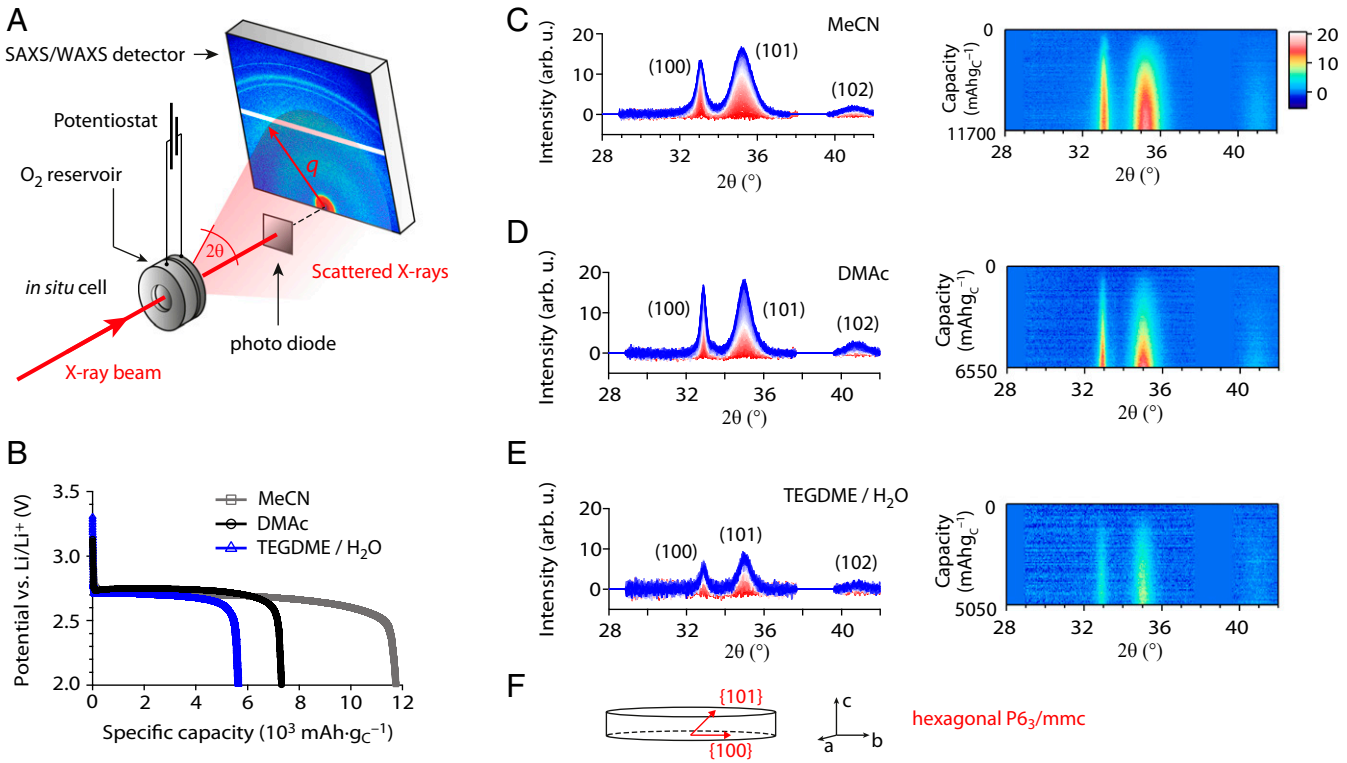

Fig. 1. In situ SAXS/WAXS experiments. (*A*) A sketch of the in situ SAXS/WAXS set-up. (*B*) Cathode potential versus specific capacity for full galvanostatic discharge during in situ SAXS/WAXS of carbon black electrodes in 1 M LiTFSI with MeCN, DMAc, and TEGDME/H_2O at 180 μA · cm_{geom}^{-2}. (*C–E*) The corresponding in situ WAXS intensities as a function of the scattering angle 2θ for galvanostatic discharge in MeCN (*C*), DMAc (*D*), and TEGDME/H_2O (*E*) electrolyte. Li_2O_2 (100), (101) and (102) peaks are indicated. Note the steadily evolving Li_2O_2 crystal phase and the difference in the (100) and (101) peak widths (see also *SI Appendix*, Fig. S5). (*F*) The orientation of the lattice vectors within the thin, disk-like Li_2O_2 crystallites, with its larger extensions normal to the crystal's *c*-axis.

modeled and measured scattering curves. The fit yields the Li_2O_2 morphology evolution in real space.

This combined experimental and modeling approach is powerful for several reasons. First, the model of the porous carbon is obtained from the same experiment (SAXS). Second, also sophisticated Li_2O_2 growth models with explicit physical input could be used that can be dealt with computationally. Third, explicit physical input of a corresponding model could be quantified and validated by structural experimental data. In this work, all used Li_2O_2 phase evolution models are fully empirical. Multiscale models (57, 58) with explicit physical input [e.g., kinetic Monte Carlo to model crystal growth (59)] would allow a more direct validation of mechanistic hypothesis and could be either run independently or, if computationally feasible, synergistically combined with in situ SAXS according to the algorithm in Fig. 2.

Li_2O_2 Product Growth and Electrolyte Solvation. With this method in hand, we examine the in situ SAXS data from above in the carbon black electrode with MeCN, DMAc, and TEGDME/H_2O electrolytes during galvanostatic discharge (Fig. 3). The MeCN SAXS data show the formation of a distinct correlation peak with a maximum around 1.75 nm^{-1}, suggesting ordered structures with a repeating unit of $2\pi/q_{peak} \cong 3.6$ nm (Fig. 3*A*). Reversibility upon charge underlines that the vast majority of the SAXS intensity changes originate from Li_2O_2 formation/dissolution (*SI Appendix*, Figs. S7 and S8). Scanning electron microscopy (SEM) (Fig. 3*C*) shows toroidal Li_2O_2 particles of ≥100 nm in size, suggesting the correlation peak to stem from parallel and ordered stacking of Li_2O_2 platelets. Similarly, in situ SAXS data of DMAc and TEGDME shows such a correlation peak (Fig. 3 *D* and *G*, respectively), albeit broader and less distinct. As confirmed by SEM images (Fig. 3 *F* and *I*), the weaker correlation points at fewer parallel Li_2O_2 layers.

Based on these qualitative statements, we developed a heuristic Li_2O_2 nucleation and growth model to extract morphological and

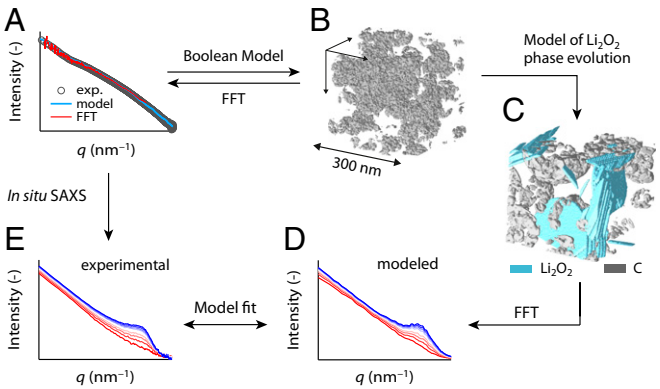

Fig. 2. In situ SAXS data analysis. (*A* and *B*) Ex situ SAXS intensity versus scattering vector length *q* of the empty carbon black electrode (*A*) and its 3D reconstructed pore structure (*B*) as obtained by fitting an intersected Boolean (Poisson) model. FFT of the 3D model into reciprocal space confirms the correctness of the derived structure. (*C–E*) Li_2O_2 is filled into the carbon pore structure with a morphology obtained from a heuristic nucleation and growth model (*C*) or any alternative algorithm (see, e.g., Fig. 4 *G* and *H*). The remaining pore space is considered electrolyte filled. FFT and spherical averaging gives modeled SAXS curves (*D*). Measured in situ SAXS curves (*E*) are then used to fit parameters of the growth model in *C* (here Li_2O_2 nucleation and growth rates) to best match modeled and measured scattering curves (*E* versus *D*).

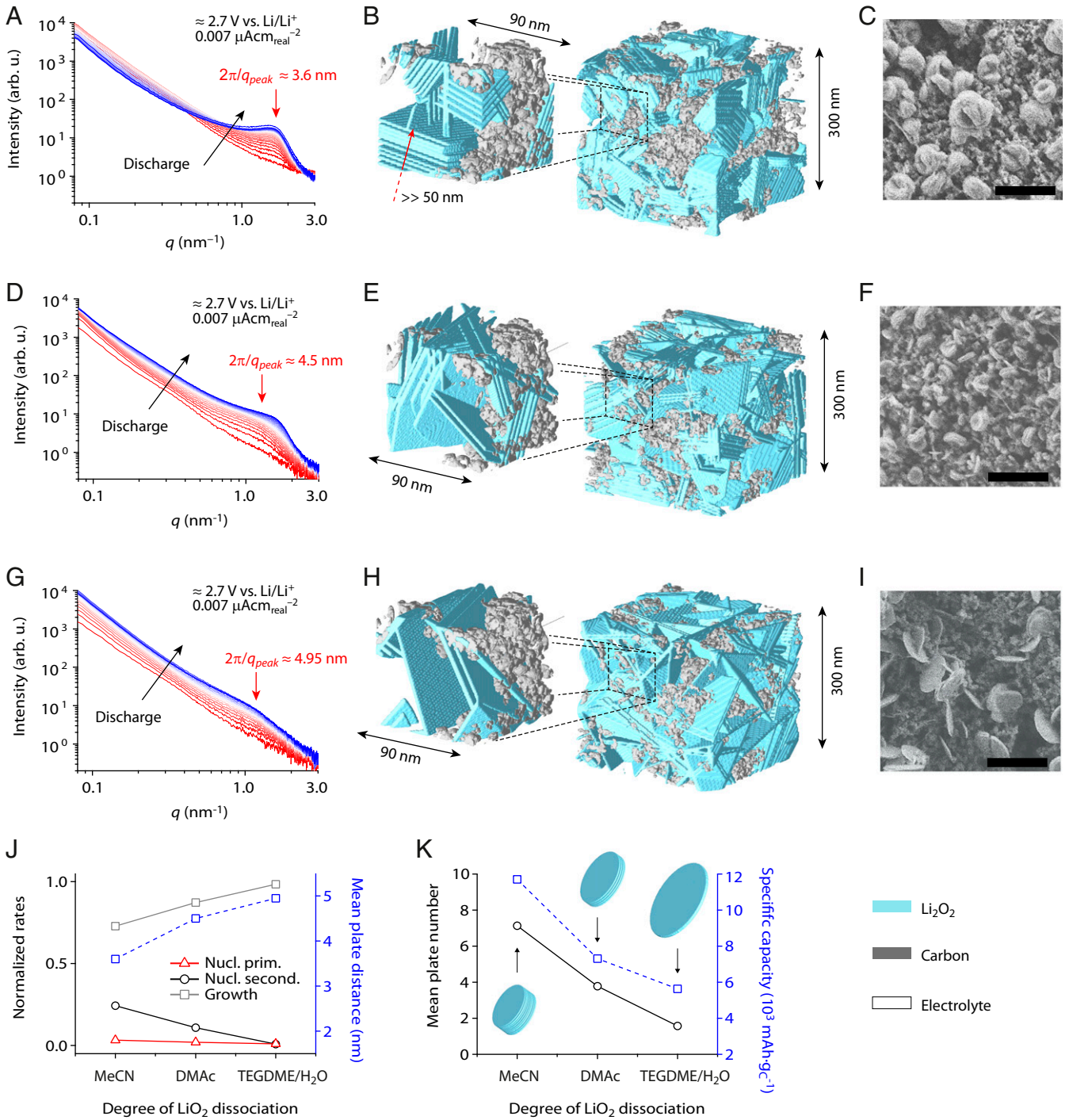

Fig. 3. In situ SAXS data and modeling results for differently LiO_2-dissociating electrolytes. (*A–C*) In situ scattering intensities versus scattering vector length q (*A*) for galvanostatic discharge of a carbon black electrode in O_2-saturated 1 M LiTFSI/MeCN at 180 μA · cm^{-2}, (from zero, red curve) to a final capacity of 11,700 mAh · g_C^{-1} (blue curve) (*A*). The 3D Li_2O_2 morphology (*B*) at a capacity of 2,200 mAh · g_C^{-1} resulting from the SAXS model fit (*SI Appendix*, Fig. S10) and a SEM image (*C*) of the electrode at the O_2 side at a capacity of 1,380 mAh · g_C^{-1} (Scale bar, 500 nm). (*D–F*) In situ scattering intensities versus scattering vector length q upon galvanostatic discharge in 1 M LiTFSI/DMAc at 180 μA · cm_{geom}^{-2} to a final capacity of 7,300 mAh · g_C^{-1} (*D*). The 3D Li_2O_2 morphology (*E*) at a capacity of 2,200 mAh · g_C^{-1} resulting from the SAXS model fit (*SI Appendix*, Fig. S10) and an SEM image (*F*) of the electrode at the O_2 side at a capacity of 1,380 mAh · g_C^{-1} (Scale bar, 500 nm). (*G–I*) In situ scattering intensities versus scattering vector length q upon galvanostatic discharge in 1 M LiTFSI/TEGDME + 4,000 ppm H_2O at 180 μA · cm_{geom}^{-2} to a final capacity of 6,350 mAh · g_C^{-1} (*G*). The 3D Li_2O_2 morphology (*H*) at a capacity of 2,200 mAh · g_C^{-1} resulting from the SAXS model fit (see *SI Appendix*, Fig. S10) and an SEM image (*I*) of the electrode at the O_2 side at a capacity of 1,380 mAh · g_C^{-1} (scale bar, 500 nm). (*J*) Normalized primary nucleation, secondary nucleation, and growth rates, as well as mean Li_2O_2 plate/layer distance (blue) as a function of the degree of LiO_2 dissociation. (*K*) Mean number of plates per Li_2O_2 stack (black) and specific capacity (blue) versus degree of LiO_2 dissociation.

kinetic information from the in situ SAXS data following the strategy presented in Fig. 2. We make three assumptions: 1) Li_2O_2 forms via solution growth, 2) Li_2O_2 crystalizes in thin, disk-like platelets, and 3) with a certain probability, platelets stack parallel on top of each other. Solution growth is known to form parallel platelets (often as toroids) (17, 18, 22, 23). Three rates govern the morphology: 1) primary nucleation of new Li_2O_2 platelets, 2) secondary nucleation of parallel platelets on top of existing ones, and 3) growth of existing platelets (*SI Appendix*, Fig. S9). Primary nucleation considers homogenous nucleation in solution only. As Li_2O_2 platelets partially engulf carbon black particles, we expect no significant difference in the SAXS intensities if heterogeneous nucleation on the carbon surface would be specifically considered. Details and limitations of the model are given in *Materials and Methods* and *SI Appendix*, Supplementary Notes 2 and 3, respectively.

Modeled best-fit morphologies for the three electrolytes are visualized in 3D and on 2D cross-sections in Fig. 3 *B*, *D*, and *G* and *SI Appendix*, Figs. S10–S13. The reasonably good fit quality between the model-derived and -measured SAXS curves indicate the 3D model morphologies to be representative of the real Li_2O_2 deposits. Fitting the MeCN data reveals the distinct correlation peak at ∼1.75 nm^{-1} to stem from a highly ordered stack of plates with stack sizes and plate expansion beyond 50 nm, the largest feature size resolvable with the given SAXS range. The model confirms that the weaker correlation with growing dissociation stems from thicker and fewer Li_2O_2 stacks (Fig. 3 *E* and *H*). Hence, nucleation decreases and growth increases.

Quantitative dependencies of model-derived parameters on the three electrolytes are given in Fig. 3 *J* and *K*. They stem from modeled best-fit real space morphologies along the depth of discharge (Fig. 3 *B*, *E*, and *H*) showing lower plate ordering as LiO_2 dissociation increases. High plate ordering in MeCN results from a large secondary nucleation rate (i.e., the rate at which new parallel plates nucleate on existing ones) (Fig. 3*J*, black trace). In contrast, the small nucleation rates in TEGDME/H_2O cause growth to dominate as confirmed in the SEM (Fig. 3*K*), which shows few but widely expanding flat layers. Fewer larger particles as solvation energies increase are also in accord with previous work (17, 23). Growing LiO_2 dissociation further manifests itself in layer distances increasing from 3.6 to 4.5 and 5 nm (Fig. 3*J*, blue trace) and a markedly decreasing mean number of parallel plates from 7.1 to 4 and 1.6 (Fig. 3*K*). The dropping plate ordering/larger size correlates with the concurrently decreasing capacity.

Absence of a Li–O_2 Surface Mechanism. Interestingly, galvanostatic discharge at low overpotentials (∼2.7 V versus Li/Li^+) reveals Li_2O_2 plates and stacks of plates with sizes beyond 100 nm, even in the poorly solvating MeCN electrolyte, which was expected to show poor capacity and Li_2O_2 surface films growing on top of the carbon. To check whether the expected Li_2O_2 surface film would be present at high discharge overpotentials (and currents), we did potentiostatic discharge at 2.1 V versus Li/Li^+. Similar to the galvanostatic in situ SAXS data, a correlation peak around 2.0 nm^{-1} appears (Fig. 4*A*), albeit broader, which points at fewer parallel Li_2O_2 layers. This peak remains constantly at 2.0 nm^{-1} as seen in the relative SAXS intensity change (SAXS intensities normalized by SAXS intensity at $t = 0$) versus time (right black arrow in Fig. 4*B*). Therefore, this peak cannot stem from particles with a growing surface layer. The latter would show a significant shift of the correlation peak from high q (small particles) to lower q (larger particles). The constant position reflects the constant mean distance of parallel Li_2O_2 plates. Also, the very high capacity of more than 4,000 mAh $\cdot$ g_C^{-1} after only 6.5 h discharge (*SI Appendix*, Fig. S14) as well as the WAXS data (Fig. 4*C* and *SI Appendix*, Fig. S15) is in line with relatively small but densely packed Li_2O_2 platelets rather than a few nm thin passivating surface film. Notably, in SEM, the discharged and pristine electrodes appear hardly distinguishable (Fig. 4*F* and *SI Appendix*, Fig. S16). Similar SEM images have been reported before and interpreted as a proof for conformal coating via the surface mechanism (17, 22, 23, 60). In a first approximation, however, the in situ SAXS data do not indicate any carbon surface coating.

Modeling the SAXS data allows to assign them clearly to surface or solution growth, confirming stacked parallel plates to be the main feature of the high-overpotential data. The (solution) nucleation and growth model confirms the broader correlation peak at ∼2.0 nm^{-1} to indicate less plates per Li_2O_2 stack compared to galvanostatic discharge (Fig. 4 *D* and *E* and *SI Appendix*, Figs. S17 and S18), and the intensity minimum around 0.5 nm^{-1} together with the broad hump around 0.2 nm^{-1} reveals small Li_2O_2 particles with a mean width around 16 nm. This intensity hump shifts toward lower q at larger depths of discharge (left black arrow in Fig. 4*B*), indicating ongoing growth of Li_2O_2 particles (i.e., increasing Li_2O_2 stack sizes). While the spatial resolution of SAXS is high enough to resolve the size and layered nature of the Li_2O_2 crystallites, in SEM they are hardly distinguishable from carbon black electrodes (Fig. 4*F*). Previously, lack of SEM spatial resolution has created the impression of conformal Li_2O_2 coatings in poorly solvating electrolytes. Here we find that even these electrolytes form Li_2O_2 at high current densities and low potential via solution growth.

To further corroborate the absence of the Li_2O_2 surface film, we calculated SAXS intensities for a hypothetical Li_2O_2 surface coating (Fig. 4 *G* and *H*). We now modeled the Li_2O_2 growth by a Monte Carlo algorithm (*Materials and Methods*) and calculated the hypothetical scattering curves by FFT. Since the X-ray scattering contrast of Li_2O_2 and carbon is similar, a conformal Li_2O_2 coating would seemingly increase the carbon particle size in terms of X-ray scattering (Fig. 4*H*). This results in a distinct SAXS intensity increase at low q only (Fig. 4*G*). Note that the layered structures explain the change over the entire range including low q in Fig. 4 *A* and *D*. Considering the nice fit between solution growth model and experimental data (*SI Appendix*, Fig. S17) and the high sensitivity of the low q intensity increase, even a small fraction of concurrent surface mechanism is highly unlikely. Alternative SAXS data interpretation is further ruled out in *SI Appendix*, Supplementary Note 4.

In summary, all in situ SAXS/WAXS data together with SEM and discharge capacities show Li_2O_2 crystallites and particles beyond 50 to 100 nm in size. A Li_2O_2 surface film is absent to a capacity relevant extent at all stages of discharge. This is true for both poorly and highly solvating electrolytes as well as high overpotentials (and currents). This suggests that the surface mechanisms with two consecutive electron transfers is widely absent under these conditions (although the exact maximum thickness of a Li_2O_2 surface coating depends on defect concentration, potential, porosity, and applied current density). In other words, SEM data together with in situ SAXS/WAXS in MeCN electrolyte and the high discharge capacities are fully consistent with nucleation and growth of Li_2O_2 platelets via solution-mediated disproportionation down to voltages where cell death occurs.

Solution discharge in weakly solvating electrolytes contradicts previous understanding that associated LiO_2 (clearly dominating in MeCN) would be insoluble. We probed for soluble superoxide with rotating ring-disk electrode (RRDE) measurements using the lithium bis(trifluoromethanesulfonyl)imide (LiTFSI)/MeCN electrolyte (Fig. 4 *I–K* and *SI Appendix*, Fig. S19). Currents from ∼0.05 to 10 μA $\cdot$ cm^{-2} were applied to the disk with the ring at ∼3.6 V versus Li/Li^+. Around 20% of the disk-generated superoxide were detected at the ring at 0.05 μA $\cdot$ cm^{-2} and values dropping to ∼5% at higher currents. Less than 100% superoxide detected at the ring do not imply respective partition between surface and solution mechanism but indicate fast disproportionation during the transit between disk and ring (Fig. 4*K*). Evidence comes from SEM images of the rotating electrode after prolonged

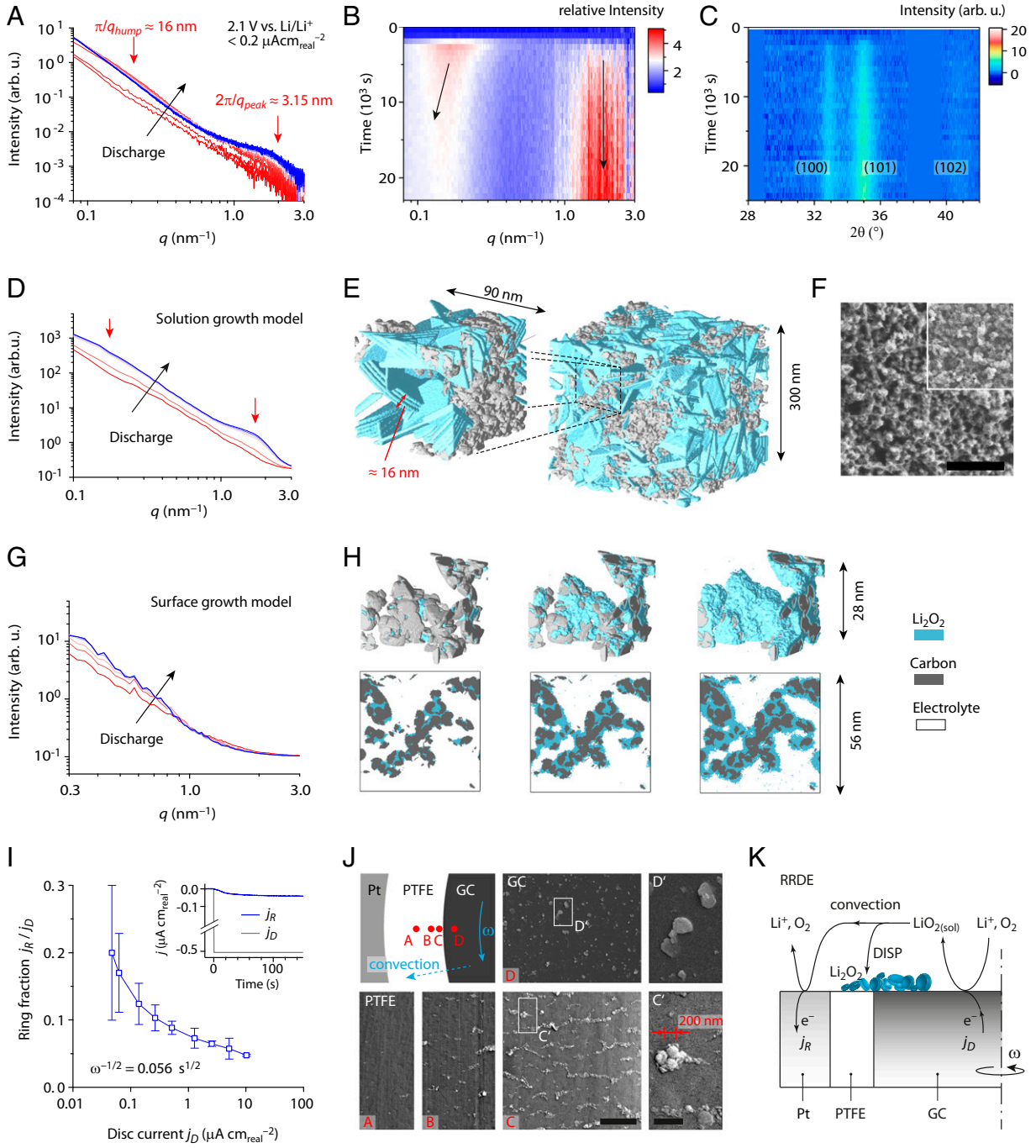

Fig. 4. Absence of a surface mechanism during Li_2O_2 formation. (*A*–*C*) In situ SAXS/WAXS intensities versus scattering vector length *q* upon potentiostatic discharge of a KB electrode in O_2-saturated 1 M LiTFSI/MeCN at 2.1 V versus Li/Li^+ (from zero, red curve) to a final capacity of ~4,000 mAh · g_C^{-1} (blue curve) (*A*). Relative SAXS intensities (normalized by the first SAXS intensity at open circuit voltage) versus time during potentiostatic discharge (*B*). The corresponding in situ WAXS intensities as a function of the scattering angle 2θ and time, with the Li_2O_2 (100), (101), and (102) peaks indicated (*C*). Modeled SAXS intensities (*D*) of the solution growth model (heuristic nucleation and growth model) up to a capacity of 3,400 mAh · $g_C^{-1}$and the corresponding 3D Li_2O_2 morphology (*E*) at a capacity of 1,630 mAh · g_C^{-1}. The SAXS model fit is shown in *SI Appendix*, Fig. S17. SEM image (*F*) of the electrode at the O_2 side at a capacity of 1,430 mAh · g_C^{-1} (Scale bar, 500 nm). The small Li_2O_2 structures shown in *F* are hardly distinguishable from the pristine carbon black (*Inset*, *Top Right*) and could be misinterpreted as Li_2O_2 surface coating. (*G* and *H*) Li_2O_2 grown as a conformal 4 nm thick film on carbon (*H*) using a Monte Carlo–based model visualized at three depths of discharge in 3D (*Top*) and by 2D cross-sections (*Bottom*). Corresponding hypothetical SAXS curves for the surface grown Li_2O_2 (*G*). Given the limited size of the 3D lattice models, the q-range of solution and surface growth model SAXS intensities are different compared to the experimental SAXS intensities. (*I*–*K*) RRDE data with 0.1 M LiTFSI/MeCN and galvanostatic disk current. The ring was held at ~3.6 V versus Li/Li^+, and the disk current density j_D was varied between 0.047 and 10.2 μA · cm_{real}^{-2}. The ring current density j_R is corrected for collection efficiency ($j_R = -i_R/N_0$). *I* shows the collected fraction j_R/j_D as a function of disk current j_D at 3,000 min^{-1} (insert: example for j_R and j_D over time) and (*J*) the collected fraction j_R/j_D as a function of rotation rate for three different disk currents j_D. (*J*) SEM images of discharged ring-disk electrode in 0.1 M LiTFSI/MeCN with j_D = 0.14 μA · cm_{real}^{-2} for 18 h (discharge capacity of 2.56 μAh · cm_D^{-2}) at a rotation rate of 800 min^{-1}. Li_2O_2 particles are deposited on the GC disk electrode and on the insulating PTFE with decaying density as the distance from the disk edge grows. [Scale bars, 2.5 μm (500 nm in C′ and D′)]. (*K*) A sketch of the reaction mechanism leading to Li_2O_2 deposition on the insulating PTFE spacer of the RRDE.

discharge (Fig. 4*J*). Li_2O_2 particles deposit outside the rotating glassy carbon (GC) disk on the polytetrafluoroethylene (PTFE) spacer with quickly decaying density as the distance from the disk edge grows (images A to C′ in Fig. 4*J*). Li_2O_2 particles at the insulating PTFE confirm Li_2O_2 nucleation and growth via solution-mediated disproportionation, the decaying density fast disproportionation. Disproportionation to form Li_2O_2 particles is also evident at the GC; similar to the PTFE, particle sizes were 100s of nm (Fig. 4*J*) or 10s of nm at somewhat higher current and steady GC substrate (*SI Appendix*, Fig. S20). Particles of such sizes cannot form via the surface mechanism, particularly not on PTFE. These data give evidence of associated LiO_2 to be soluble, mobile, and to disproportionate from solution to Li_2O_2 particles.

Discussion

The absence of a Li_2O_2 conformal coating formed via the surface mechanism in both poorly solvating (low DN) electrolytes and at high overpotential has important consequences. Contrary to previous beliefs, the capacity is limited by mass transport of reactive species rather than electronic transport limitation through a passivating Li_2O_2 coating. During discharge, the increasingly tortuous transport path in the Li_2O_2–carbon cavities self-accelerates tortuosity increase, finally causing end-of-discharge by mass transport limitation (O_2 and Li^+) toward the electrode surface (combined with some degree of surface blocking by Li_2O_2 particles touching the carbon, Fig. 5*A*). Mass transport limitation is reasoned theoretically (34) and comparable to the effect of pore blocking by NaO_2 crystals in Na–O_2 batteries (61). Absence of surface growth even in MeCN and at high overpotentials/high discharge currents implies these factors to be limiting in all electrolytes. Note that mass transport limitation here does not mean macroscopic O_2 transport limitation across the 10s of μm thick carbon electrode. Electron microscopy shows that Li_2O_2 particles form equally in size and number density on both the separator and O_2 reservoir side of the electrode for galvanostatic discharge (*SI Appendix*, Fig. S4).

Mass transport rather than electronic transport limitation implies that the species mobility controls, next to current density and LiO_2 dissociation, the Li_2O_2 morphology and hence discharge capacities. The very high species mobilities in MeCN likely explain the unexpectedly high discharge capacity in combination with the high surface area carbon black electrode. At the same time, the Li_2O_2 plates are arranged more highly ordered compared to the other electrolytes, enabling a higher degree of Li_2O_2 pore filling before the tortuosity becomes too high.

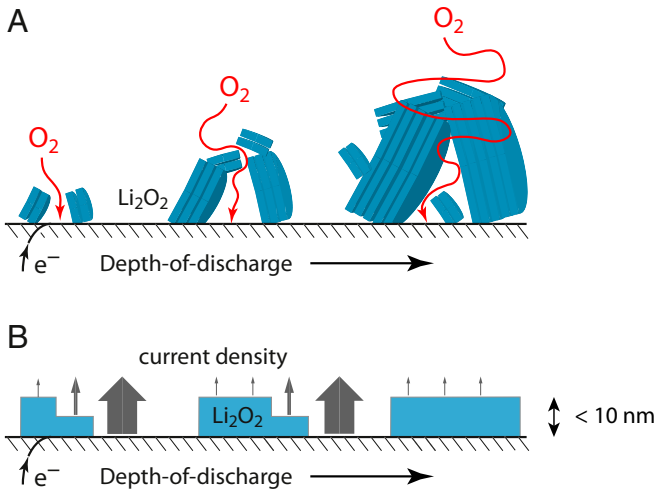

Fig. 5. Morphology evolution and capacity limitations upon solution or surface discharge. (*A*) Build-up of an increasingly tortuous particulate Li_2O_2 layer upon solution discharge, imposing growing mass transport limitations. Given the known role of adsorbed LiO_2 on existing Li_2O_2 (69), we believe that the solution mechanism also implies significant LiO_2 transport via the surface of existing Li_2O_2 platelets. (*B*) Li_2O_2 layer thickness evolution upon surface discharge. The increase of resistance with layer thickness (exponential in the case of tunneling) strongly favors further growth at open or thinner layers, eventually leading to self-leveling of the Li_2O_2 surface layer thickness.

To demonstrate the importance of current density, we discharged porous electrodes made of low surface area GC powder at the same geometric current density as the carbon black electrodes, resulting in ∼1,000-fold higher current density (3.5 μA · cm_{real}^{-2}). The discharge capacities clearly follow the order as predicted in the literature with similar current densities (22): the stronger the LiO_2 dissociation, the higher the discharge capacity (*SI Appendix*, Fig. S3). This implies that the often quoted correlation "the larger the Li_2O_2 particle size, the larger the capacity" is only true for planar or low surface area electrodes (such as GC). In nanoporous carbon black electrodes, not only the particle size but primarily the pore filling determines the capacity. Hence, the increased species mobilities (O_2, O_2^-, and Li^+), the highly ordered Li_2O_2 stacks, and the fact that pore filling and not solely the particle size determines capacity, explains the improved performance of MeCN with KB.

Given that a Li_2O_2 conformal coating is absent for the reputedly most prototypical conditions, the question arises whether the Li_2O_2 conformal coating is absent under all practically relevant conditions. Our data with different electrolytes and at different discharge potentials would imply so. Given that the surface mechanism with two consecutive electron transfers was until now widely considered to form film-like coatings, our results suggest that oxygen reduction in poorly solvating electrolytes does not take place to any capacity-relevant extent via twofold electrochemical one-electron transfer. While the maximum film thickness may vary slightly with applied current density and potential, the overall morphology obtained from the surface mechanism should be film like (specifically on a flat substrate, as used in Fig. 4*J* and *SI Appendix*, Fig. S20). Tunneling causes the local film resistance to increase exponentially with increasing thickness (46). Reduction rates must hence be much faster at spots with none or lower film thickness than at spots with already thicker film (57), resulting in self leveling (Fig. 5*B*). Even if electronic conduction rather than tunneling prevails (41) and the conductivity were higher due to defects (40, 43, 62), individual, large particles (>50 nm) as shown in Figs. 3 and 4 on (nearly) bare carbon surface would leave the question why there is no growth at the bare surface in between. Significant RRDE ring fractions and Li_2O_2 deposited on the insulating PTFE spacer of the RRDE imply that Li_2O_2 forms to the widest extent via solution-mediated LiO_2 disproportionation, even under conditions previously considered prototypical for surface growth.

Exclusive solution discharge would require reconsidering the currently accepted Li–O_2 reduction mechanism. What is the real evidence remaining for the surface mechanism to take place? Much support for the assumption of surface routes has been drawn from 1) end of discharge at calculated compact Li_2O_2 layers of ≤7 nm, estimated to be the maximum tunneling thickness (25, 26) and 2) RRDE or quartz crystal microbalance measurements that have shown mobile and seemingly immobile superoxide in strongly and poorly solvating electrolytes, respectively (18, 19, 22). Yet, theoretically, a pure solution mechanism could explain all these observations. First, seemingly electron-blocking ∼7 nm layers were obtained at high current ≥1 μA · cm_{BET}^{-2}. As shown in Fig. 4, Li_2O_2 forms at already 10-fold lower current density in small particles that are indistinguishable from carbon black particles in SEM and easily misinterpreted as conformal layer (Fig. 4 *D*–*F*). Second, seemingly immobile superoxide was concluded from only small to negligible RRDE ring current when several 100 μA · cm^{-2} disk currents were applied

CHEMISTRY

(18, 22). This could be explicable by the fast $LiO_{2(sol)}$ disproportionation in poorly solvating electrolytes (63) preventing $LiO_{2(sol)}$ from reaching the ring (Fig. 4 *I–K*). More in-depth studies on superoxide solubility and disproportionation kinetics are necessary to conclusively answer the here shown discrepancies and to possibly derive a revised $Li–O_2$ reaction mechanism.

On a wider perspective, the here developed method of in situ SAXS together with sophisticated data evaluation is established as a powerful in situ method for battery systems and beyond. It expands the accessible length scales of existing structure-sensitive methods, such as X-ray tomography (13), with a seamless resolution from subnanometers to submicrometers. The data analysis approach allows to directly validate the structural evolution obtained with modeling attempts (16, 57, 59) using in situ scattering data (54). The example of Li_2O_2 deposition serves to demonstrate that seamless structural information all the way from atomic to micrometric scales holds the key to important mechanistic detail (here second e^- transfer versus disproportionation). The methodology can hence elucidate otherwise hardly accessible reaction mechanisms and growth processes in complex multiphase systems such as batteries, hybrid supercapacitors, fuel cell catalysts, and beyond.

Materials and Methods

Materials. LiTFSI from SOLVIONIC was dried under reduced pressure for 24 h at 140 °C. MeCN and DME were distilled under Ar over CaH_2. DMAc and TEGDME were distilled under vacuum. All solvents were further dried and stored over freshly activated molecular sieves (type 4 Å).

The water content of the electrolytes was determined by Karl Fischer titration using a Methrom 851 Titrando and found to be ≤30 ppm (details, *SI Appendix*, Supplementary Note 1). The BET areas of GC spherical powder (Aldrich) and KetjenBlack (AkzoNobel) were determined by N_2 gas adsorption and found to be 1.3 $m^2 \cdot g^{-1}$ and 1,398 $m^2 \cdot g^{-1}$, respectively. Electrodes were made by mixing carbon with PTFE (60 mass% suspension in water, Aldrich) at 90 : 10 (wt / wt) ratio with isopropanol. The resulting dough-like material was rolled to a 50 to 70 μm thick free standing film electrode, washed in acetone/H_2O mixture and finally dried at 120 °C under vacuum overnight. Specific surface areas, specific pore volumes, electrode densities, and total porosities of the three carbon electrodes are given in *SI Appendix*, Table S2. Partially delithiated Lithium iron phosphate (LFP) was used for the counter electrode material, which was made by mixing LFP, delithiated LFP, Super P (Timcal), and PTFE in a 62 : 17 : 11 : 10 (wt / wt) ratio with isopropanol and rolling the resulting material to a 500 μm thick free standing film electrode, washing in acetone/H_2O mixture and drying at 120 °C under vacuum overnight. All electrodes were transferred to an Ar-filled glovebox without air exposure.

Experimental. In situ SAXS measurements were conducted using custom-built in situ SAXS $Li–O_2$ cells and a SP-150 galvanostat/potentiostat (Biologic). Both electrochemical standard and in situ SAXS cells used a sandwich of carbon cathode (50 to 70 μm thick, 8 mm in diameter), an electrolyte-soaked Whatman GF/A separator, and an oversized partially delithiated LFP counter electrode (500 μm thick, 12 mm in diameter). The custom-designed in situ $Li–O_2$ cell consisted of Al grid current collectors, LFP counter electrode, and a carbon cathode in contact with a Nickel foam for oxygen gas supply. A hole within the partially delithiated LFP electrode ensured that the X-ray beam hits the cathode only (64). The hole has a diameter of 2 mm to avoid detrimental effects of increased Li^+ diffusion pathways in the cell. In situ SAXS/WAXS experiments were performed at a laboratory SAXS instrument (SAXSpoint 2.0, Anton Paar GmbH) using Cu-K_α radiation and a Dectris EIGER2 R 1M area detector. Simultaneous SAXS and WAXS patterns were recorded by alternately measuring for 15 min (5 min for potentiostatic discharge) at 530 mm and 100 mm sample-to-detector distance, respectively. In addition, proof-of-principle in situ SWAXS experiments were performed at the Austrian SAXS beamline (65) at the synchrotron radiation source Elettra in Trieste using an X-ray wavelength of 0.154 nm and a Dectris Pilatus 1M detector (SAXS) and a Pilatus 100K detector (WAXS) for data collection. All recorded SAXS patterns were azimuthally averaged and normalized by transmission values. The SAXS background intensity was recorded separately for each cell after removing the cathode. The averaged and normalized background intensity was then subtracted from all recorded in situ SAXS curves. In situ WAXS data were corrected by subtracting a linear background from the azimuthally averaged 2D WAXS pattern.

SEM was carried out on a Zeiss Ultra 55 FEG-SEM (field emission gun-SEM) using a classical Everhart–Thornley and a high-efficiency in-lens SE detector. To minimize beam damage, all images were recorded with an acceleration voltage of 0.8 kV at lowest achievable emission current. The different image contrasts of the used SE detectors are based on different detector positions and detector efficiencies. For Fig. 4*J*, first platinum (Pt) was sputtered to minimize the electron beam–induced damage and to avoid charging at the PTFE. A high vacuum sputtering system Leica EM ACE600 was used to deposit 1.6 nm Pt. To ensure high purity of the Pt layer, the sputtering system was purged three times with Ar gas prior to sputtering. A FEG-SEM Carl Zeiss MERLIN VP Compact was used. The signal was detected using an in-column in-lens secondary electron detector and by in-chamber HE-SE2 Everhart–Thornley detector. The Pt layer allowed to use 5 kV accelerating voltage in combination with a 10 μm aperture. Higher accelerating voltage increased the contrast between the surface and the crystals, improving subsequent data analysis. Energy-dispersive spectroscopy was acquired using an EDAX Octane Elite Super 70 mm^2 controlled by APEX 1.5 Advanced Software and equipped with an SiN window.

RRDE measurement was performed inside an Ar-filled glovebox using a rotator (model MSR) and an RRDE with 5 mm GC disk and a Pt ring with 6.5 (7.5) mm inner (outer) diameter (all Pine research). A SP-300 potentiostat/galvanostat (Biologic) was used for the measurements. Measurements were performed in a cylindrical glass cell with narrow upper opening through which the shaft, a $Li_{1-x}FePO_4$ reference electrode and counter electrode on a stainless-steel grid, and a tube for O_2 were inserted. After O_2 saturation by direct bubbling, the electrolyte was further bubbled during the entire measurement. The electrode was polished before every experiment using 0.05 mm alumina slurry in isopropanol, rinsed with MeCN and dried under vacuum. A solution of 2 mM ferrocene in 0.1 M tetrabutyl ammonium TFSI in MeCN were used to determine the collection efficiency N_0 of the ring.

SAXS Data Analysis.

Carbon pore model generation. The computer-generated 3D pore morphology is obtained from the experimental SAXS intensity of the bare carbon electrodes using intersected Boolean models (56). The method involves a model fit to the measured SAXS intensity and uses the resulting fit parameters as an input to generate a statistically representative 3D pore structure on a 3D lattice (with $400 \times 400 \times 400$ voxels and a voxel size of $0.75 \times 0.75 \times 0.75$ nm).

The model generation requires some a priori knowledge about the pore structure (e.g., from SEM), since the solution of the model fit is not unique. Visually, SEM images and the carbon structure obtained from SAXS correspond well in *SI Appendix*, Fig. S6. Pore size distributions from N_2 gas adsorption are given in *SI Appendix*, Fig. S21.

The derivation of the real space pore structure via intersected Boolean models is described in more detail elsewhere (56). In short, a Boolean model is based on spherical grains randomly distributed in space. Here, we define $N = 5$ classes of randomly distributed grains with radius R_i. A voxel in the 3D lattice belongs to the solid (carbon) phase if the voxel can be attributed to a grain for each of the five classes. The geometrical covariogram of randomly distributed spherical grains i reads

$$K_i(r) = \frac{4\pi}{3} R_i{}^3 \left(1 - \frac{r}{2R_i}\right)^2 \left(1 - \frac{r}{4R_i}\right) \Theta(2R_i - r), \quad [1]$$

where r is the real space coordinate, and $\Theta()$ the Heaviside step function, being 1 for a positive argument and 0 otherwise. The solid covariance $C_{11}(r)$ is the probability that a stick with length r, with random position and direction has both of its ends in the solid phase of the two-phase pore structure. It can be calculated from the geometrical covariogram $C_{11}(r)$.

$$C_{11}(r) = \prod_{i=1}^{N} \phi_{0,i}{}^2 (\exp[\theta_i K_i(r)] - 1) + (1 - \phi_{0,i})^2. \quad [2]$$

$\phi_{0,i}$ is the pore volume fraction of a specific class of grains i and equals $\exp(-\theta_i 4/3\pi R_i{}^3)$, where θ_i is the number density of grains in the simulation box. The number density of grains θ_i is adjusted such that $\phi_1 = \prod(1\text{-}\phi_{0,i})$ equals the total volume fraction of the solid phase. The model scattering intensity $I(q)$ is obtained by numerically integrating

$$I(q) = K \cdot \phi_1(1 - \phi_1)(\Delta\rho)^2 \int_0^\infty \gamma(r) \frac{\sin(qr)}{qr} 4\pi r^2 dr, \quad \text{with} \quad \gamma(r) = \frac{C_{11}(r) - \phi_1{}^2}{\phi_1(1 - \phi_1)}. \quad [3]$$

This model scattering intensity is fitted to the measured intensity, with the grain sizes R_i, the number density of grains θ_i, and the prefactor in Eq. **3** being fitting parameters. We take the total carbon volume fraction $\phi_1 = 0.11$ from the

density of the dry electrode (given in *SI Appendix*, Table S2). It is calculated via $\phi = V_{\text{spec, pore}}/(V_{\text{spec, pore}} + 1/\rho_{\text{skeleton}})$, where the carbon density was assumed with 2.05 g · cm^{-3} and the specific pore volume calculated from $V_{\text{spec, pore}} = 1/\rho_{\text{dry}} - 1/\rho_{\text{skeleton}}$. The obtained fit parameters are used to generate the intersected Boolean model on a 3D lattice. The real space pore structure is obtained by intersecting the 3D structure of each class of grains and by fulfilling periodic boundary conditions. A 3D electron density map of the porous carbon is generated by weighting the obtained real-space structure by the mean scattering length density levels of the two phases (carbon skeleton and pores). We use $1.74 \cdot 10^{11}$ cm^{-2} (corresponding to a mass density of 2.05 g · cm^{-3}) for the carbon phase and zero for the pore phase. A numerical FFT of the electron density map and a subsequent spherical averaging of the squared amplitude of the FFT yields the corresponding scattering curve and by such verifies the correctness of the derived structure with respect to the model fit (red curve, *SI Appendix*, Fig. S6*A*) with respect to the modeled SAXS intensity.

Heuristic Li_2O_2 nucleation and growth model. The 3D carbon structure can be filled with Li_2O_2 particles based on a heuristic algorithm as described below. The algorithm is based on three assumptions: 1) Li_2O_2 crystalizes in form of thin, disk-like plates with a predefined plate thickness. This shape can be traced back to the anisotropic surface energy of the Li_2O_2 crystal structure and is experimentally observed in the large difference of (100) and (101) WAXS peak widths (Fig. 2*B*); 2) Li_2O_2 is formed via solution-mediated growth only. This assumption is based on the large gravimetric capacity cells using high surface area carbons, such as KB (Fig. 1); and 3) with a certain probability, Li_2O_2 plates stack on top of each other with a predefined plate distance and in a parallel arrangement. The order in between parallel plates causes correlation peaks in the SAXS pattern.

We simulate the discharge process in the carbon cathode by filling the carbon structure with Li_2O_2 in steps of 3,375 or 562.5 nm^3 (i.e., 3,375 nm^3 is the smallest volume unit for modeling of galvanostatic measurements and 562.5 nm^3 for potentiostatic measurements). Both memory and computational time restrict the 3D lattice of the nucleation and growth model to a size of $400 \times 400 \times 400$ voxels. To adequately model the Li_2O_2 particle size on the one hand and sufficiently resolve the ~2 nm thick Li_2O_2 plates on the other hand, we choose a voxel size of 0.75 nm^3.

The Li_2O_2 structure evolves by the following: 1) Placing the smallest volume unit of a Li_2O_2 plate at a random position with random orientation in the pore space (primary nucleation); 2) placing a Li_2O_2 plate on top of an existing plate with parallel arrangement (secondary nucleation). The diameter of the added plate is the same as the diameter of the existing plate; and 3) expanding the diameter of existing Li_2O_2 plates (growth). Li_2O_2 plates in a given Li_2O_2 stack always grow simultaneously. Prior to each nucleation and growth step, one of the three options is chosen with a certain probability (Monte Carlo–based draw). These values are related to the main model input parameters: primary nucleation rate, secondary nucleation rate, and growth rate. Nucleation and growth probabilities are obtained by multiplying the input rates with a weighting factor accounting for 1) the availability of empty pore space (primary nucleation), 2) the total area of Li_2O_2 plane sites (secondary nucleation), and 3) the total area of Li_2O_2 plate edge sites (growth). To account for long-range disorder in between parallel stacked plates, the next-neighbor distance in the case of secondary nucleation is varied following a Gaussian distribution. Equivalently, for primary and secondary nucleation, the predefined plate thickness is varied with Gaussian probability. More details can be found in *SI Appendix*, Fig. S22 and Supplementary Note 2.

The phase evolution model does not consider for carbon pore swelling. Li_2O_2 discs can partially engulf carbon particles, presuming that particles do not effectively shadow other regions of empty pore space (*SI Appendix*, Fig. S23). Hence considered Li_2O_2–carbon structural correlations are small.

To generate the modeled SAXS curves, the real-space carbon + Li_2O_2 + electrolyte structure is weighted by the corresponding scattering length densities. We used $1.74 \cdot 10^{11}$ cm^{-2} for carbon, $1.92 \cdot 10^{11}$ cm^{-2} for Li_2O_2, and $7.77 \cdot 10^{10}$ cm^{-2}, $9.65 \cdot 10^{10}$ cm^{-2}, and $9.13 \cdot 10^{10}$ cm^{-2} for MeCN, DMAc, and TEGDME + 4,000 ppm H_2O, respectively. The resulting 3D electron density map was then Fourier transformed via FFT, and the modeled SAXS curve was obtained via spherical averaging of the squared amplitude reciprocal space map (54, 55, 66). To make experimental and model scattering curves comparable, we multiply the model scattering curve by an empirically determined (instrumental) constant K and a constant background caused by the electrolyte and carbon structure factor (64) and determined from the experimental SAXS intensity at 3 nm$^{-1} < q < 5$ nm^{-1}. The impact of the carbon skeleton density value and the carbon black structure on the modeled scattering intensity is discussed in *SI Appendix*, Supplementary Note 3.

To fit the modeled scattering intensity to the experimental data, we generated nine model scattering curves with increasing depths of discharge (in steps of 400 mAhg$_C^{-1}$ assuming 100% Li_2O_2 yield) for a given set of fit parameters (i.e., growth rates, nucleation rates, mean values, and SDs of plate distance, see *SI Appendix*, Table S3). The sum of squared residuum values $r^2_j(q_i)$ for all q_i and depths of discharge j ($M = 9$ DoDs, between 200 and 3,600 mAhg$_C^{-1}$, *SI Appendix*, Fig. S10) was calculated via

$$R_{DoD} = \sum_{j}^{M=9}\sum_{i}^{N} r^2_j(q_i) = \sum_{j}^{M=9}\sum_{i}^{N}\left(I_{\text{exp, }j}(q_i) - I_{\text{mod, }j}(q_i)\right)^2 \Big/ \left(I_{\text{exp, }j}(q_i)\right)^2. \quad [4]$$

The modeled scattering intensity $I_{\text{mod, }j}(q_i)$ was fitted to the experimental scattering curve $I_{\text{exp, }j}(q_i)$ in the range 0.1 nm$^{-1} < q_i < 3.0$ nm^{-1}, with N $q_i$values. The model scattering curve and the corresponding fit parameters are chosen by minimizing the error sum of all depths of discharge R_{DoD} for a given set of fit parameters. The fitting was realized by sampling the parameter space on a reasonably coarse grid with defined constraints and calculating the sum of squared deviations for each of these points. Parameters with minimum error sum were taken as the solution. Sampling the entire parameter space, rather than using optimization algorithms allowed 1) getting an overview about local minima and 2) understanding the effect of specific parameter variations on the scattering intensity.

Extremely high currents for potentiostatic discharge cause inhomogeneous Li_2O_2 formation across the cathode (*SI Appendix*, Fig. S16). The degree of Li_2O_2 filling as calculated from electrochemical measurements can hence not be assigned to the actual Li_2O_2 filling at the irradiated spot on the cathode. We found that modeled scattering curves with Li_2O_2 occupancy that relate to 0, 326, 1,954, 2,280, 2,605, and 2,930 mAhg$_C^{-1}$ best fit the measured in situ SAXS curves at mean cathode capacities of 0, 600, 2,160, 2,310, 2,380, and 2,570 mAhg$_C^{-1}$ (model versus experimental SAXS curves see *SI Appendix*, Fig. S17). Best-fit parameters for potentiostatic discharge were determined by comparing these sets of scattering curves. Limitations and possible sources of error are discussed in *SI Appendix*, Supplementary Note 3.

Monte Carlo surface growth model. To model Li_2O_2 surface growth, we generated 3D phases that uniformly cover the carbon surface using a Monte Carlo–based algorithm and calculated scattering curves via FFT of the obtained 3D structures. The algorithm does not intend to include real physical interactions. The goal is to understand how SAXS intensities change upon coating the carbon electrode with Li_2O_2, which could, in principle, be achieved by other methods as well (67).

First, 3D carbon models are randomly filled with Li_2O_2 voxels (Li_2O_2 beads), where the quantity is defined by a given depth of discharge. Then Li_2O_2 beads are rearranged according to a Metropolis algorithm (68). To account for the higher particle formation probability close to the carbon surface, we introduce an empirical attractive potential that exponentially decays with distance to the carbon surface. A pragmatic method to generate such empirical potential on the 3D lattice is by convoluting the real space carbon volumetric data obtained from the intersected Boolean models with a Gaussian function. We use a 3D Gaussian image filter and weight the resulting 3D lattice data by an appropriate factor to obtain the empirical potential. The surface energy is minimized by accounting for Ising-type nearest-neighbor interactions. The total energy of the system reads

$$E = \sum_{i}^{N} E_{\text{emp.}}(x_i,\ y_i, z_i) - \gamma_{Li_2O_2}\sum_{i}^{N}\sum_{j}^{M}\sigma_i\sigma_j\ , \quad [5]$$

with $E_{\text{emp.}}$ being the empirical energy term accounting for the attractive interaction between Li_2O_2 beads and the carbon surface and $\gamma_{Li_2O_2}$ accounting for the gain in surface energy if neighboring voxels belong both to the Li_2O_2 phase. σ_i and σ_j equal +1 or −1 if the voxel is occupied by Li_2O_2 or electrolyte, respectively. N corresponds to the number of Li_2O_2 beads and M to the number of nearest neighbors. In line with the Metropolis algorithm, the new energy is calculated after each Monte Carlo move and compared to the old one. The move is accepted if the new energy is lower and accepted with a Boltzmann probability if the new energy is higher. After the desired morphologies have been obtained and equilibration is convenient, the simulation is stopped.

To minimize computational time and increase the spatial resolution, here we use a 3D lattice consisting of $160 \times 160 \times 160$ voxels with a voxel size of $0.35 \times 0.35 \times 0.35$ nm. Equivalent to the heuristic nucleation and growth model, all phases are weighted by their corresponding electron densities to obtain the 3D electron density map of the structure. FFT and spherical averaging yields the modeled scattering curves.

Data Availability. All study data are included in the article and/or *SI Appendix*.

ACKNOWLEDGMENTS. S.A.F. and C.P. are indebted to the European Research Council under the European Union's Horizon 2020 research and innovation program (Grant Agreement No. 636069), the Austrian Federal Ministry of Science, Research and Economy, and the Austrian Research Promotion Agency (Grant No. 845364). We acknowledge A. Zankel and H. Schroettner for support with SEM measurements. C.P. thanks N. Kostoglou, C. Koczwara, M. Hartmann, and M. Burian for discussions on gas sorption analysis, C++ programming, Monte Carlo modeling, and in situ SAXS experiments, respectively. We thank S. Stadlbauer for help with Karl Fischer titration, R. Riccò for gas sorption measurements, and acknowledge Graz University of Technology for support through the Lead Project LP-03. Likewise, the use of SOMAPP Lab, a core facility supported by the Austrian Federal Ministry of Education, Science and Research, the Graz University of Technology, the University of Graz, and Anton Paar GmbH is acknowledged. S.A.F. is indebted to Institute of Science and Technology Austria (IST Austria) for support. This research was supported by the Scientific Service Units of IST Austria through resources provided by the Electron Microscopy Facility.

1. M. Eder, S. Amini, P. Fratzl, Biological composites-complex structures for functional diversity. *Science* **362**, 543–547 (2018).
2. C. P. Grey, J. M. Tarascon, Sustainability and in situ monitoring in battery development. *Nat. Mater.* **16**, 45–56 (2016).
3. V. Wood, X-ray tomography for battery research and development. *Nat. Rev. Mater.* **3**, 293–295 (2018).
4. J. W. Choi, D. Aurbach, Promise and reality of post-lithium-ion batteries with high energy densities. *Nat. Rev. Mater.* **1**, 16013 (2016).
5. D. Aurbach, B. D. McCloskey, L. F. Nazar, P. G. Bruce, Advances in understanding mechanisms underpinning lithium–air batteries. *Nat. Energy* **1**, 16128 (2016).
6. Q. Pang, X. Liang, C. Y. Kwok, L. F. Nazar, Advances in lithium–sulfur batteries based on multifunctional cathodes and electrolytes. *Nat. Energy* **1**, 16132 (2016).
7. N. Mahne, O. Fontaine, M. O. Thotiyl, M. Wilkening, S. A. Freunberger, Mechanism and performance of lithium-oxygen batteries–A perspective. *Chem. Sci. (Camb.)* **8**, 6716–6729 (2017).
8. Y.-C. Lu *et al*., Lithium–oxygen batteries: Bridging mechanistic understanding and battery performance. *Energy Environ. Sci.* **6**, 750–768 (2013).
9. E. Mourad *et al*., Singlet oxygen from cation driven superoxide disproportionation and consequences for aprotic metal–O_2 batteries. *Energy Environ. Sci.* **12**, 2559–2568 (2019).
10. Y. Wang *et al*., A solvent-controlled oxidation mechanism of Li_2O_2 in lithium-oxygen batteries. *Joule* **2**, 2364–2380 (2018).
11. S. Zhang *et al*., On the incompatibility of lithium-O_2 battery technology with CO_2. *Chem. Sci. (Camb.)* **8**, 6117–6122 (2017).
12. M. Ebner, F. Marone, M. Stampanoni, V. Wood, Visualization and quantification of electrochemical and mechanical degradation in Li ion batteries. *Science* **342**, 716–720 (2013).
13. P. Pietsch, V. Wood, X-ray tomography for lithium ion battery research: A practical guide. *Annu. Rev. Mater. Res.* **47**, 451–479 (2017).
14. M. G. Boebinger, J. A. Lewis, S. E. Sandoval, M. T. McDowell, Understanding transformations in battery materials using in situ and operando experiments: Progress and outlook. *ACS Energy Lett.* **5**, 335–345 (2020).
15. J. Nelson Weker, M. F. Toney, Emerging in situ and operando nanoscale X-ray imaging techniques for energy storage materials. *Adv. Funct. Mater.* **25**, 1622–1637 (2015).
16. A. Torayev, P. C. M. M. Magusin, C. P. Grey, C. Merlet, A. A. Franco, Importance of incorporating explicit 3D-resolved electrode mesostructures in Li–O_2 battery models. *ACS Appl. Energy Mater.* **1**, 6433–6441 (2018).
17. N. B. Aetukuri *et al*., Solvating additives drive solution-mediated electrochemistry and enhance toroid growth in non-aqueous Li-O_2 batteries. *Nat. Chem.* **7**, 50–56 (2015).
18. D. G. Kwabi *et al*., Controlling solution-mediated reaction mechanisms of oxygen reduction using potential and solvent for aprotic lithium-oxygen batteries. *J. Phys. Chem. Lett.* **7**, 1204–1212 (2016).
19. D. Sharon *et al*., Mechanistic role of Li^+ dissociation level in aprotic Li-O_2 battery. *ACS Appl. Mater. Interfaces* **8**, 5300–5307 (2016).
20. D. G. Kwabi *et al*., Experimental and computational analysis of the solvent-dependent O_2/Li^+-O_2^- redox couple: Standard potentials, coupling strength, and implications for lithium-oxygen batteries. *Angew. Chem. Int. Ed. Engl.* **55**, 3129–3134 (2016).
21. C. Li *et al*., Aprotic Li–O_2 battery: Influence of complexing agents on oxygen reduction in an aprotic solvent. *J. Phys. Chem. C* **118**, 3393–3401 (2014).
22. L. Johnson *et al*., The role of LiO_2 solubility in O_2 reduction in aprotic solvents and its consequences for Li-O_2 batteries. *Nat. Chem.* **6**, 1091–1099 (2014).
23. C. M. Burke, V. Pande, A. Khetan, V. Viswanathan, B. D. McCloskey, Enhancing electrochemical intermediate solvation through electrolyte anion selection to increase nonaqueous Li-O_2 battery capacity. *Proc. Natl. Acad. Sci. U.S.A.* **112**, 9293–9298 (2015).
24. J. S. Hummelshøj *et al*., Communications: Elementary oxygen electrode reactions in the aprotic Li-air battery. *J. Chem. Phys.* **132**, 071101 (2010).
25. P. Albertus *et al*., Identifying capacity limitations in the Li/oxygen battery using experiments and modeling. *J. Electrochem. Soc.* **158**, A343–A351 (2011).
26. V. Viswanathan *et al*., Electrical conductivity in Li_2O_2 and its role in determining capacity limitations in non-aqueous Li-O_2 batteries. *J. Chem. Phys.* **135**, 214704 (2011).
27. C. O. Laoire, S. Mukerjee, K. M. Abraham, E. J. Plichta, M. A. Hendrickson, Elucidating the mechanism of oxygen reduction for lithium-air battery applications. *J. Phys. Chem. C* **113**, 20127–20134 (2009).
28. K. B. Knudsen, T. Vegge, B. D. McCloskey, J. Hjelm, An electrochemical impedance spectroscopy study on the effects of the surface- and solution-based mechanisms in Li-O_2 cells. *J. Electrochem. Soc.* **163**, A2065–A2071 (2016).
29. B. Horstmann *et al*., Rate-dependent morphology of Li_2O_2 growth in Li-O_2 batteries. *J. Phys. Chem. Lett.* **4**, 4217–4222 (2013).
30. J. Liu, S. Khaleghi Rahimian, C. W. Monroe, Capacity-limiting mechanisms in Li/O_2 batteries. *Phys. Chem. Chem. Phys.* **18**, 22840–22851 (2016).
31. N. Mahne *et al*., Singlet oxygen generation as a major cause for parasitic reactions during cycling of aprotic lithium–oxygen batteries. *Nat. Energy* **2**, 17036 (2017).
32. J. Wandt, P. Jakes, J. Granwehr, H. A. Gasteiger, R.-A. Eichel, Singlet oxygen formation during the charging process of an aprotic lithium-oxygen battery. *Angew. Chem. Int. Ed. Engl.* **55**, 6892–6895 (2016).
33. Y. Wang, Y.-R. Lu, C.-L. Dong, Y.-C. Lu, Critical factors controlling superoxide reactions in lithium–oxygen batteries. *ACS Energy Lett.* **5**, 1355–1363 (2020).
34. S. Lau, L. A. Archer, Nucleation and growth of lithium peroxide in the Li-O_2 battery. *Nano Lett.* **15**, 5995–6002 (2015).
35. A. Torayev *et al*., Stochasticity of pores interconnectivity in Li-O_2 batteries and its impact on the variations in electrochemical performance. *J. Phys. Chem. Lett.* **9**, 791–797 (2018).
36. J. Huang *et al*., Probing the reaction interface in Li-oxygen batteries using dynamic electrochemical impedance spectroscopy: Discharge-charge asymmetry in reaction sites and electronic conductivity. *J. Phys. Chem. Lett.* **9**, 3403–3408 (2018).
37. J. Lu, T. Wu, K. Amine, State-of-the-art characterization techniques for advanced lithium-ion batteries. *Nat. Energy* **2**, 17011 (2017).
38. T. Liu *et al*., Current challenges and routes forward for nonaqueous lithium-air batteries. *Chem. Rev.* **120**, 6558–6625 (2020).
39. B. D. McCloskey, R. Scheffler, A. Speidel, G. Girishkumar, A. C. Luntz, On the mechanism of nonaqueous Li–O_2 electrochemistry on C and its kinetic overpotentials: Some implications for Li–air batteries. *J. Phys. Chem. C* **116**, 23897–23905 (2012).
40. F. Tian, M. D. Radin, D. J. Siegel, Enhanced charge transport in amorphous Li_2O_2. *Chem. Mater.* **26**, 2952–2959 (2014).
41. A. C. Luntz *et al*., Tunneling and polaron charge transport through Li_2O_2 in Li–O_2 batteries. *J. Phys. Chem. Lett.* **4**, 3494–3499 (2013).
42. M. D. Radin, D. J. Siegel, Charge transport in lithium peroxide: Relevance for rechargeable metal–air batteries. *Energy Environ. Sci.* **6**, 2370–2379 (2013).
43. W. T. Geng, B. L. He, T. Ohno, Grain boundary induced conductivity in Li_2O_2. *J. Phys. Chem. C* **117**, 25222–25228 (2013).
44. Y. Yin, R. Zhao, Y. Deng, A. A. Franco, Compactness of the lithium peroxide thin film formed in Li-O_2 batteries and its link to the charge transport mechanism: Insights from stochastic simulations. *J. Phys. Chem. Lett.* **8**, 599–604 (2017).
45. C. Yang *et al*., Unexpected Li_2O_2 film growth on carbon nanotube electrodes with CeO_2 nanoparticles in Li-O_2 batteries. *Nano Lett.* **16**, 2969–2974 (2016).
46. J. G. Simmons, Generalized formula for the electric tunnel effect between similar electrodes separated by a thin insulating film. *J. Appl. Phys.* **34**, 1793–1803 (1963).
47. Z. Li *et al*., Understanding the electrochemical formation and decomposition of Li_2O_2 and LiOH with *Operando* X-ray diffraction. *Chem. Mater.* **29**, 1577–1586 (2017).
48. S. Ganapathy *et al*., Nature of Li_2O_2 oxidation in a Li-O_2 battery revealed by operando X-ray diffraction. *J. Am. Chem. Soc.* **136**, 16335–16344 (2014).
49. B. M. Gallant *et al*., Influence of Li_2O_2 morphology on oxygen reduction and evolution kinetics in Li–O_2 batteries. *Energy Environ. Sci.* **6**, 2518–2528 (2013).
50. R. R. Mitchell, B. M. Gallant, Y. Shao-Horn, C. V. Thompson, Mechanisms of morphological evolution of Li_2O_2 particles during electrochemical growth. *J. Phys. Chem. Lett.* **4**, 1060–1064 (2013).
51. L. Zhong *et al*., In situ transmission electron microscopy observations of electrochemical oxidation of Li_2O_2. *Nano Lett.* **13**, 2209–2214 (2013).
52. Y. Mo, S. P. Ong, G. Ceder, First-principles study of the oxygen evolution reaction of lithium peroxide in the lithium-air battery. *Phys. Rev. B* **84**, 205446 (2011).
53. P. Fratzl *et al*., "Diffracting "stacks of cards" - some thoughts about small-angle scattering from bone" in *Scattering Methods and the Properties of Polymer Materials*, N. Stribeck, B. Smarsly, Eds. (Springer, Berlin Heidelberg, 2005), pp. 33–39.
54. C. Prehal *et al*., Quantification of ion confinement and desolvation in nanoporous carbon supercapacitors with modelling and in situ X-ray scattering. *Nat. Energy* **2**, 16215 (2017).
55. C. Prehal *et al*., A carbon nanopore model to quantify structure and kinetics of ion electrosorption with in situ small-angle X-ray scattering. *Phys. Chem. Chem. Phys.* **19**, 15549–15561 (2017).
56. C. J. Gommes, Stochastic models of disordered mesoporous materials for small-angle scattering analysis and more. *Microporous Mesoporous Mater.* **257**, 62–78 (2018).

57. Y. Yin, A. Torayev, C. Gaya, Y. Mammeri, A. A. Franco, Linking the performances of Li–O_2 batteries to discharge rate and electrode and electrolyte properties through the nucleation mechanism of Li_2O_2. *J. Phys. Chem. C* **121**, 19577–19585 (2017).
58. Y. Yin, C. Gaya, A. Torayev, V. Thangavel, A. A. Franco, Impact of Li_2O_2 particle size on Li-O_2 battery charge process: Insights from a multiscale modeling perspective. *J. Phys. Chem. Lett.* **7**, 3897–3902 (2016).
59. V. Thangavel *et al*., A three dimensional kinetic Monte Carlo model for simulating the carbon/sulfur mesostructural evolutions of discharging lithium sulfur batteries. *Energy Storage Mater.* **24**, 472–485 (2019).
60. B. D. Adams *et al*., Current density dependence of peroxide formation in the Li–O_2 battery and its effect on charge. *Energy Environ. Sci.* **6**, 1772–1778 (2013).
61. N. B. Aetukuri *et al*., Ion pairing limits crystal growth in metal–oxygen batteries. *ACS Energy Lett.* **3**, 2342–2348 (2018).
62. A. Dunst, V. Epp, I. Hanzu, S. A. Freunberger, M. Wilkening, Short-range Li diffusion vs. long-range ionic conduction in nanocrystalline lithium peroxide Li_2O_2—the discharge product in lithium-air batteries. *Energy Environ. Sci.* **7**, 2739–2752 (2014).
63. Y. Zhang *et al*., Amorphous Li_2O_2: Chemical synthesis and electrochemical properties. *Angew. Chem. Int. Ed. Engl.* **55**, 10717–10721 (2016).
64. C. Prehal *et al*., Tracking the structural arrangement of ions in carbon supercapacitor nanopores using in situ small-angle X-ray scattering. *Energy Environ. Sci.* **8**, 1725–1735 (2015).
65. H. Amenitsch *et al*., First performance assessment of the small-angle X-ray scattering beamline at ELETTRA. *J. Synchrotron Radiat.* **5**, 506–508 (1998).
66. K. Schmidt-Rohr, Simulation of small-angle scattering curves by numerical Fourier transformation. *J. Appl. Cryst.* **40**, 16–25 (2007).
67. C. Gommes, Three-dimensional reconstruction of liquid phases in disordered mesopores using in situ small-angle scattering. *J. Appl. Cryst.* **46**, 493–504 (2013).
68. D. P. Landau, K. Binder, *A Guide to Monte Carlo Simulations in Statistical Physics* (Cambridge University Press, 2014).
69. J. Yang *et al*., Evidence for lithium superoxide-like species in the discharge product of a Li-O_2 battery. *Phys. Chem. Chem. Phys.* **15**, 3764–3771 (2013).